Title: Methane oxidation dynamics in a karst subterranean estuary

Authors: David Brankovits[a,b,1,*] and John W. Pohlman[b]

[a] Department of Marine Biology, Texas A&M University at Galveston, Galveston, TX 77553, USA;

[b] U.S. Geological Survey, Woods Hole Coastal and Marine Science Center, Woods Hole, MA 02543, USA;

[1] Present address: Department of Marine Chemistry and Geochemistry, Woods Hole Oceanographic Institution, Woods Hole, MA 02543, USA;

*corresponding author

Email addresses: D.B. (dbrankovits@whoi.edu), J.W.P. (jpohlman@usgs.gov)

ABSTRACT

Chemical gradients between fresh, brackish and saline waters shape biogeochemical reactions and organic matter transformation within subterranean estuaries. In the Yucatán Peninsula's karst subterranean estuary (KSE), methane and dissolved organic matter generated during the anaerobic decomposition of tropical forest vegetation are transported into flooded cave networks where microbial consumption greatly reduces their concentrations in the groundwater. To test the hypothesis that chemoclines associated with salinity gradients of the KSE are sites of methane oxidation, we obtained methane concentration and $\delta^{13}C$ profiles of unprecedented vertical resolution from within a fully-submerged cave system located 6.6 km inland from the coastline using the 'OctoPiPi' (OPP) water sampler. Along a 12-24 cm thick low-salinity-halocline at ~4.5 m water depth, salinity increased from fresh to brackish (0.2 to 1.8 psu), methane concentrations decreased, and $\delta^{13}C$ values increased, as expected for microbial methane oxidation. The underlying brackish water had elevated oxygen concentrations compared to the always anoxic freshwater, suggesting that aerobic methane oxidation is the dominant process facilitating methane consumption. By contrast, as salinity increased from 1.8 to 36 psu through a 24-36 cm thick high-salinity-halocline between the meteoric lens and the saline groundwater at ~20 m water depth, methane concentrations and $\delta^{13}C$ values were constant. Conservative mixing and kinetic isotope models incorporating the methane data confirm a hotspot for microbial methane oxidation at the low-salinity-halocline. At least 98% of methane originating in the anoxic freshwaters was removed before its transport via channelized flow towards the coastline. These findings provide novel insight into the spatial constraints of methane dynamics within a karst subterranean estuary.

INTRODUCTION

Subterranean estuaries occur globally within carbonate, siliciclastic and basaltic coastlines, where the mixing of fresh and marine-derived groundwater creates a biogeochemical reaction zone that alters the chemical composition of submarine groundwater discharge (Moore, 1999, 2010). Multiple studies have demonstrated that global submarine groundwater discharge is the dominant source of some dissolved terrestrial materials to the oceans (e.g., Kwon et al., 2014; Lee et al., 2010; Taniguchi et al., 2002). Methane oxidation (Schutte et al., 2016) and other biogeochemical processes (Kroeger and Charette, 2008; Moore, 2010; Santoro et al., 2008) in subterranean estuaries have been shown to reduce the concentrations of methane and other chemical constituents transported from siliciclastic settings to the coastal ocean. Carbonate coastal aquifers are distinct from those in siliciclastic coastlines because the permeable geologic setting often contains conduits (cave passages) that enhance hydraulic transport and exchange of material with the coastal ocean within many island platforms and coastal regions (Beddows et al., 2007; Martin et al., 2012; Perry et al., 2002). The high permeability of coastal karst terrane allows the subterranean estuary to extend kilometers inland (van Hengstum et al., 2011) (Fig. 1), which impacts the carbon cycle (Brankovits et al., 2017; Pohlman, 2011; Pohlman et al., 1997) and regional water resources (Bauer-Gottwein et al., 2011; Vesper et al., 2001). Karst platforms account for ~25% of all coastlines (Ford and Williams, 2013) and ~12% of submarine groundwater discharge globally (Beck et al., 2013). Furthermore, transport of dissolved material from carbonate platforms account for a substantial percentage of certain inorganic trace element inputs in the world ocean (e.g., up to 33% for strontium and up to 28% for uranium; Gonneea et al., 2014), suggesting that elemental cycling within coastal aquifers has an impact far beyond the subterranean environment. For all these reasons, biogeochemical processes occurring within karst subterranean estuaries (KSEs) are likely to impact coastal ocean carbon budgets as well.

Density stratification within siliciclastic (Kroeger and Charette, 2008; Moore, 2010; Santoro, 2010; Schutte et al., 2016) and karstic (Gonzalez et al., 2011;

Humphreys, 1999; Pohlman, 2011; Socki et al., 2002) coastal aquifers creates sharp physicochemical gradients that affect organic matter cycling. Analogous transitional zones are found in estuaries (Chanton and Lewis, 1999), hydrothermal vents (Corliss et al., 1979; Paull et al., 1984), deep-sea cold seeps (Levin, 2005), and meromictic (permanently stratified) lakes (Bastviken et al., 2008). The exchange of material across these gradients creates biogeochemical hotspots that also shape ecosystem function. Numerous studies have characterized the hydrogeology (Beddows et al., 2007; Coutino et al., 2017; Kambesis and Coke, 2013; Perry et al., 2002) and invertebrate zoology (Alvarez et al., 2015; Humphreys, 1999; Iliffe and Kornicker, 2009) associated with the salinity mixing zone (halocline) between the meteoric lens and saline groundwater in KSEs (Fig. 1). Biogeochemical studies suggest organic matter degradation and associated cycling of nitrogen and sulfur species are enhanced at the meteoric-saline halocline in sinkholes and interior caves (Humphreys, 1999; Pohlman, 2011; Socki et al., 2002). High-resolution vertical sampling across the salinity gradient of an eutrophic open sinkhole revealed changes in the chemistry and microbiology (Seymour et al., 2007). However, a similar approach has not been applied to characterize the cycling of carbon along chemoclines that occur in the greater aquifer, within the flooded oligotrophic caves.

The Yucatán Peninsula's 165,000 km^2 carbonate platform contains vast networks of cave passages (Kambesis and Coke, 2013) flooded by the meteoric freshwater and saline groundwater (Fig. 1). The environment supports a rich community of anchialine fauna (Iliffe and Kornicker, 2009; Stock et al., 1986) consisting primarily of cave-adapted crustaceans (Alvarez et al., 2015) specifically adapted to the oligotrophic cave environment (Bishop et al., 2015; Iliffe and Kornicker, 2009; Stock et al., 1986). In this setting, far from open sinkholes, a subterranean microbial loop (inset circle on Fig. 1) transfers carbon from methane (CH_4) and dissolved organic carbon (DOC) formed by decomposition of terrestrial vegetation into the anchialine food web (Brankovits et al., 2017). Here, the water column in the flooded caves is characterized by distinct fresh-, brackish- and saline-water layers, limited particulate organic matter, and high

concentrations of methane and other dissolved organic matter in the freshwater portion of the water column, near the ceiling of the caves. Methane accumulation and consumption in the shallow portion of the aquifer are seasonally persistent processes driven by rainfall and hydrology (Brankovits et al., 2018). Nevertheless, details about the location and geochemical conditions that permit methane oxidation within the cave conduits remain uncertain.

Biogeochemical processes that balance methane production and consumption within stratified aquatic or marine environments regulate the transfer of methane to the atmosphere (Bastviken et al., 2011; Boetius and Wenzhofer, 2013), where it is a greenhouse gas 25 times more potent than carbon dioxide on a 100-year time scale (IPCC, 2014; Reeburgh, 2007). Moreover, methane plays a prominent role in the ecosystem function of aquatic habitats (Bastviken et al., 2003; Deines et al., 2009; DelVecchia et al., 2016; Devlin et al., 2015; Grey, 2016), including the Yucatán's karst aquifer (Brankovits et al., 2017). In meromictic lakes and reservoirs where water masses are permanently stratified, 20-60% of the organic carbon produced in surface waters is transported to the anoxic hypolimnion (Bastviken et al., 2008). A fraction of this carbon is transformed into methane by sedimentary or water column methanogenesis (Wetzel, 2001). The methane is either oxidized and returned to the lake's carbon cycle (Bastviken et al., 2004) where it has been shown to contribute carbon and energy to the limnic food web (Bastviken et al., 2003; He et al., 2015), or it may transfer to the atmosphere (Bastviken et al., 2011). Density stratification affects methane dynamics, including methane removal, in subterranean estuaries within siliciclastic (Schutte et al., 2016) and karstic (Brankovits et al., 2017, 2018) settings. As groundwater is being transported in the shallow aquifer seaward, the above-mentioned biogeochemical processes will affect the methane concentrations of discharging submarine groundwater, an important source of methane to coastal waters (Burnett et al., 2006; Cable et al., 1996; Taniguchi et al., 2002). Because karstic coastlines account for ~25% of the global coastal geomorphology (Ford and Williams, 2013), investigating carbon cycling and methane dynamics

associated with sharp salinity gradients in KSEs will likely provide insight into an important component of the coastal carbon cycle.

In this study, we investigate the role of redox interfaces associated with salinity mixing zones within the meromictic coastal aquifer of the Yucatán Peninsula's karstic platform. As part of these efforts, we test the hypothesis that methanotrophy occurs at an anoxic-hypoxic interface separating the fresh and brackish water masses. A high-resolution water sampling device developed for this study was used to obtain pristine cm-scale vertical chemical profiles across haloclines within cave passages of the KSE. Concentrations and stable carbon isotopic values of methane collected along the full salinity spectrum were used to construct conservative mixing and kinetic isotope models to differentiate changes in concentrations and carbon isotope ratios imposed by physical mixing between water masses from those caused by microbial production and consumption of methane. This study has the potential to define the constraints of methane removal from the groundwater prior to its expulsion into the coastal ocean, evasion into overlying tropical soils, and, ultimately, the atmosphere.

MATERIALS AND METHODS

Study sites and sampling periods

Field campaigns were conducted in January 2015 and January 2016 in flooded caves accessed through the Cenote Bang sinkhole (20° 12.62' N 87° 30.064' W). Cenote Bang is part of the Ox Bel Ha cave system (with >240 km mapped cave passages) that underlies a seasonally dry tropical forest, the dominant natural vegetation in the region (White and Hood, 2004), south of Tulum, Quintana Roo, Mexico (Fig. 2a-b). This region is located on the Caribbean coast of the Yucatán Peninsula where the low elevation karst terrain lacks surface streams and rivers due to the high permeability of the limestone bedrock (e.g., Beddows et al., 2007; Perry et al., 2002). Here, more than 1,000 km of mapped cave networks are found within the coastal region of the Holbox fracture zone (Bauer-Gottwein et al., 2011; Kambesis and Coke, 2013). These cave passages are densely distributed within the inland portion of the subterranean estuary over an area

153 (~1,100 km^2) comparable to surface estuarine systems, such as Galveston Bay
154 (~1,400 km^2), the 7th largest estuary in the US (Brankovits et al., 2017). Cenote Bang
155 provides access to a complex meromictic subterranean aquatic environment with a
156 shallow (<4.5 m) meteoric freshwater (FW) layer (<0.5 psu) that is always anoxic (0-15
157 μM); an intermediate (4.5-20 m) meteoric brackish water (BW) layer (0.5-30.0 psu) that
158 varies from anoxic to hypoxic (1-30 μM) depending on the sampling event; and a deep
159 (>20 m) saline groundwater (SG) layer (30.0-35.0 psu) that typically has the highest
160 dissolved oxygen concentrations (45-55 μM) (Brankovits et al., 2017; Pohlman and
161 Brankovits, 2017). Here, the salinity/density interface between the FW and BW is
162 referred to as the low-salinity-halocline and the interface between the BW and SG is
163 referred to as the high-salinity-halocline. Continuous flow in the BW maintains a
164 constant hydrological transport mechanism towards the coast. Although the seasonally
165 dynamic hydrological conditions affect flow velocity and halocline thickness, the water
166 column in the conduits is stratified year-round (Brankovits et al., 2018). In both years,
167 sampling was conducted during the dry season which typically lasts from December to
168 April/May (Curtis et al., 1996; Kottek et al., 2006). Dissolved oxygen concentrations
169 were lower in 2016 than they were in 2015 (Fig. 2d). The caves investigated in this study
170 had no visible evidence of direct or indirect human alterations; therefore, they are
171 presumed to represent a pristine habitat. Nevertheless, infiltration of wastewater into the
172 groundwater, resulting from common sewage disposal practices in the region, may
173 impact water quality both in the fresh and saline portions of the aquifer.
174
175 *Sample collection and processing*
176 Sampling was carried out on SCUBA, following diving and safety protocols
177 established by the American Academy of Underwater Sciences and the National
178 Speleological Society-Cave Diving Section. Water samples were obtained at cm-scale
179 vertical resolution across the low-salinity- and high-salinity-haloclines using the
180 OctoPiPi (OPP) water sampling system developed by the U.S. Geological Survey
181 (USGS) (Fig. 3). The OPP samplers used in this study consist of a rack of ten 60 ml

plastic syringes mounted and evenly distributed along an aluminum frame with a mechanical, spring-powered trigger-system that fills syringes when activated. An OPP with fixed 12 cm syringe spacing (Fig. 3) and another with 2.5 cm syringe spacing (the mini-OPP) were deployed during this study. The OPPs were mounted vertically across interfaces identified from depth-salinity profiles collected prior to deployment (Fig. 2) and visually confirmed during deployment. The OPPs were left in place for at least 24 hr to allow the water column to re-stratify before being triggered. The top-mount of the OPP was connected to either an inflated dive lift bag or elastic bands carefully attached to the cave ceiling. The bottom-mount was connected to 1/8" braided nylon line deployed by dive reel and attached to at least 5 kg of lead for stability. When triggered, the OPP slowly and simultaneously filled the syringes to a volume of 40-60 ml depending on OPP geometry. The 60-ml syringes were fitted with 3-way stopcocks that were closed immediately after triggering to contain the samples. Prior to deployment, the syringe assemblies were rinsed thoroughly with distilled water and completely dried.

Following OPP recovery, the syringes were transported on ice to the field lab, where they were processed within eight hours of collection following protocols described by Brankovits et al. (2017). Briefly, the 60-ml water sample was divided into subsamples for further geochemical analyses of dissolved constituents, including, but not limited to, methane, dissolved inorganic carbon, dissolved organic carbon, inorganic nutrients and ions. For the present study, chloride and sulfate ion concentrations as well as methane concentrations and $\delta^{13}C$ values are reported. Samples for ion analysis were filtered through a 0.45 µm Acrodisc® syringe filter and collected in a 2-ml plastic screw-top vial. 30-ml serum vials for methane water samples were prepared prior to sample collection by adding 0.5 ml 8 M NaOH into the empty vial as a preservative, sealing the container with 1 cm thick butyl septa, and vacating the vial of air with a vacuum pump. An unfiltered 20-ml water sample was then transferred from the syringe into the serum vial by piercing the septum with a 20-gauge syringe needle and regulating water flow with the stopcock. Water samples were stored in the fridge at 7 °C.

Geochemical analysis

Geochemical analyses were performed at the Woods Hole Oceanographic Institution (WHOI) and USGS in Woods Hole MA, USA. After balancing the headspace of the serum vial for methane analysis to 1 atmosphere with helium, headspace methane concentrations were determined using a Shimadzu 14-A gas chromatograph (GC) equipped with a flame ionization detector (FID). The gases were isothermally (50 °C) separated with a Poraplot-Q stainless steel column (8 ft x 1/8" OD) packed with 60/80 mesh and quantified against certified gas standards with a relative standard deviation (RSD) of 2.8% or less. Headspace concentrations were converted to dissolved concentrations using an established method (Magen et al., 2014). The stable carbon isotope composition of methane ($\delta^{13}C$-CH_4) from the headspace of the serum vials was determined using a Thermo-Finnigan DELTA^{Plus} XL isotope ratio mass spectrometer (IRMS) coupled to an Agilent 6890 Gas Chromatograph (GC) via a Finnigan GCCIII combustion interface. Variable volume (1-15.0 ml) gas samples, depending on concentrations, were introduced through a gas sampling valve into a 1 ml min^{-1} He carrier gas stream. Following an established method (Popp et al., 1995) with modifications, methane and other condensable gases were trapped on fused silica capillary packed with 80/100 mesh Poraplot-Q immersed in liquid nitrogen. The gases were thermally desorbed from the column at 150 °C and separated on a 30 m, 0.32 mm ID Poraplot-Q column at −40 °C prior to being oxidized to CO_2 and analyzed by IRMS. The $^{13}C/^{12}C$ ratios of methane are expressed in the standard δ-notation using tank CO_2 referenced to the Vienna Pee Dee Belemnite (VPDB) standard. The standard deviation (1 σ) of a 1% CH_4 standard analyzed at least every 8 samples was 0.3‰.

Sulfate and chloride concentrations were determined using a Metrohm 881 Compact Plus ion chromatograph (IC) equipped with a Metrosep A Supp 5-250 anion column. Samples from the FW, BW and SG were diluted by factors of 31, 61 and 101, respectively, to maintain chloride concentrations within the range of the conductivity detector. Peak areas for sulfate and chloride were quantified against equivalently diluted International Association for the Physical Sciences of the Oceans (IAPSO) standard

seawater analyzed at the beginning of the run and after every fifth sample. Chloride concentrations (mM) were converted to mg l^{-1} and multiplied by 0.0018066 to report salinity (psu). The analytical error (standard deviation) for dissolved constituents was ± 3.5% of the IAPSO (International Association for the Physical Sciences of the Oceans) standard sulfate and chloride values.

Conservative mixing calculations

Conservative mixing models were used to differentiate the roles of physical mixing from *in situ* microbial oxidation (consumption) on the concentration and isotopic composition of methane across salinity gradients. This approach has been used to investigate carbon dynamics in estuaries (Chanton and Lewis, 1999) and brine-affected marine pore waters (Pohlman et al., 2008). The conservative mixing calculations were conducted using salinity and methane data obtained from the OPP profiles similar to the approach used by Brankovits et al. (2017) using manually collected samples. Briefly, conservative mixing was calculated between salinity endmembers collected with (1) the OPP in 2015, (2) the OPP in 2016, and (3) the mini-OPP in 2016. For each calculation, endmembers included the lowest measured salinity sample in the FW and the highest measured salinity sample in the SG, using matching methane concentrations and $\delta^{13}C$ values for the samples (Supplementary Data). These calculations are represented as conservative mixing lines on the salinity-property diagrams. The area in between the reported mixing calculations is considered the general mixing field that incorporates all mixing lines, where the constituents would physically mix in the absence of biological and/or chemically mediated inputs or removal. By applying the mixing model to each deployment period, it was possible to determine the fraction of methane removed by methanotrophy along gradients where high methane in the FW mixes with lower methane in the BW (Brankovits et al., 2017).

Kinetic isotope models

To delineate if changes in the carbon isotope ratios were due to oxidation or mixing with other methane sources, the measured $\delta^{13}C$ values and concentrations of methane were incorporated into the kinetic isotope model described by Leonte et al. (2017). The approach is based on the observation that isotopic fractionation during methane oxidation causes the residual methane to become increasingly enriched with ^{13}C relative to the source value (a.k.a., the kinetic isotope effect) (Barker and Fritz, 1981; Whiticar, 1999). Coupled shifts in methane concentration and $\delta^{13}C$ values during oxidation may be described with either a "closed-system" Rayleigh isotopic fractionation model (Damm et al., 2007; Leonte et al., 2017) or an "open-system" isotope model (e.g., Kessler et al., 2006). The primary assumption of the Rayleigh model is that microbial methane oxidation is the only process altering the $\delta^{13}C\text{-}CH_4$ values following first-order reaction kinetics. This model assumes no mixing with other methane-rich waters; however, if methane inputs from alternate sources occur but are so low that the mixing does not substantially alter the $\delta^{13}C$ of the bulk methane pool, the closed-system assumption remains valid (Leonte et al., 2017). By contrast, the open-system model accounts for mixing of methane-rich waters with different methane content and $\delta^{13}C$ values, in addition to the kinetic isotope effect that occurs during oxidation. By comparing each of these models to measured $\delta^{13}C$ values and concentrations of methane released from seafloor seeps in the Hudson Canyon of the U.S. Atlantic Margin, Leonte et al. (2017) were able to distinguish methane oxidation and methane dispersion from other sources. Here, we apply a similar approach to assess methane oxidation at the low-salinity-halocline (where isotopic evidence for methane oxidation was obtained).

Equations for the Rayleigh (Eq. 1) and open-system (Eq. 2) models are:

(1) $$f_c = 1 - \left(\frac{\delta R+1000}{\delta R_0+1000}\right)^{\left(\frac{\alpha_c}{1-\alpha_c}\right)}, \text{ and}$$

(2) $$f_o = \frac{\alpha_o}{1-\alpha_o}\left(\frac{\delta R_0+1000}{\delta R+1000} - 1\right),$$

where f is the fraction oxidized, α is the isotope fractionation factor, the subscripts c and o refer to the closed- and open-system models, δR_0 is the source (or initial) δ^{13}C-CH_4 value of methane in the freshwater, and δR is the δ^{13}C-CH_4 value of each remaining sample along the gradient. δR_0 (−67.49‰) is the average δ^{13}C-CH_4 from the sample with the highest methane concentration (7,793 nM; $\delta^{13}C$ = −67.48‰) and the lowest $\delta^{13}C$ value (−67.51‰; 7,295 nM). The average concentration for those samples (C_0) is 7,544 nM, which is used to calculate the fraction methane oxidized (see Results) as described by Leonte et al. (2017).

The isotope fractionation factors for the closed-system (α_c, Eq. 3) and open-system (α_o, Eq. 4) models were obtained through linearization of Eqns. (1) and (2):

(3) $$\ln[C] = \frac{\alpha_c}{1-\alpha_c}\ln[\delta R + 1000] - \frac{\alpha_c}{1-\alpha_c}\ln[\delta R_0 + 1000] + \ln[C_0], \text{ and}$$

(4) $$C = -\frac{\alpha_o C_o(\delta R_0+1000)}{1-\alpha_o} \times \frac{1}{(\delta R+1000)} + C_0\left(\frac{\alpha_o}{1-\alpha_o} + 1\right),$$

where C is the measured CH_4 concentration for each sample. The slopes of the linear regressions for the two models ($slope_c$ and $slope_o$ on Fig. 4) were used to calculate the fraction factors. The resulting isotope fractionation factors for the closed-system model (α_c = 1.004) and open-system model (α_o = 1.024) are comparable to those from other systems (Leonte et al., 2017; Whiticar, 1999). Even though the α_o value is comparable to other studies, the open-system model is a poor linear fit for the measured dataset (Fig. 4b). In contrast, the closed-system linear model fits well the measured dataset (Fig. 4a).

RESULTS

Vertical chemical profiles

High-resolution sampling of the mixing zones revealed dramatic methane and sulfate gradients associated with the shift in salinity at the shallow, low-salinity-halocline (Fig. 5). In the FW, salinity ranged from 0.17 to 0.47 psu, with the exception a single 0.92 psu salinity value in 2015. This anomalous value is likely a sample handling or analytical artifact because it is not consistent with any of the sonde measurements

(Fig. 2). The FW had high methane concentrations (ranging from 1,272 to 7,793 nM) that were ^{13}C-depleted (ranging from −58.1‰ to −67.5‰). By contrast, the BW had oligohaline salinity (ranging from 1.81 to 1.88 psu) and lower methane concentrations (ranging from 37 to 132 nM) that were ^{13}C-enriched (ranging from −47.8‰ to −55.5‰) relative to the FW. The profile obtained in January 2015 had steeper chemical gradients and a substantially higher average methane concentration (7,187 ± 185 nM) and ^{13}C-depleted $\delta^{13}C\text{-}CH_4$ value (−67.1 ± 0.2‰) than the January 2016 profile average concentration (3,246 ± 238 nM) and $\delta^{13}C\text{-}CH_4$ value (−64.0 ± 1.3‰).

The vertical extent, or thickness, of the halocline was 12 cm in 2015 (Fig. 5a) and 24 cm in 2016 (Fig. 5b). The average depth of the halocline was 4.2 m in 2015 and 4.6 m in 2016. A higher resolution (2.5 cm) vertical profile obtained from the low-salinity-halocline with the mini-OPP provides a more detailed record of the intermediate chemical properties (Fig. 5c). In this profile, increasing salinity across the chemical gradient (from 0.74 to 1.84 psu) was associated with decreasing methane concentrations (from 1,419 to 42 nM) and increasing $\delta^{13}C\text{-}CH_4$ values (from −65.2 to −52.0‰). Although the trends were similar, chemical gradients collected with the two different samplers in 2016 (Fig. 5b-c) did not exactly match along the depth profiles. Small-scale spatial variability in cave ceiling morphology and/or overlying conditions (e.g., soil/rock-matrix and vegetation) may have affected the measured data, resulting in the observed differences.

Across the deeper high-salinity-halocline, an extreme shift in salinity and sulfate concentration was observed, but the methane concentrations and $\delta^{13}C\text{-}CH_4$ values were relatively constant (Fig. 6a-b). Salinity varied from oligohaline (as low as 1.79 psu) to mesohaline (as high as 14.38 psu) in the BW and from 31.11 to 35.95 psu in the SG. Methane concentrations ranged from 9 to 121 nM with $\delta^{13}C\text{-}CH_4$ values −44.6‰ to −57.5‰ throughout the profiles with no obvious trend that would imply methane consumption or production at the interface. Methane across the interface was higher in concentration (ranging from 50 nM to 121 nM) and more depleted (−50.4‰ to −57.5‰) in 2015 than in 2016 when concentrations ranged from 9 nM to 33 nM with more

enriched $\delta^{13}C\text{-}CH_4$ values (−44.6‰ to −50.6‰). Shifts in salinity across this halocline occurred within a 24 cm transition zone at approximately 19.80 m water depth in January 2015 (Fig. 6a) and within a 36 cm zone at approximately 20.0 m in January 2016 (Fig. 6b). Salinity varied from oligohaline (3.17 psu) to polyhaline (29.73 psu) across the 25 cm mini-OPP profile (Fig. 6c).

Across all profiles at the two haloclines, endmember salinity and sulfate values were in agreement with previous measurements using other sampling techniques (Brankovits et al., 2017, 2018), suggesting the records captured the full range of salinity in the flooded cave conduits. The sulfate concentrations measured here (0.1 to 28.9 mM) were also in agreement with previously reported values from this site (Brankovits et al., 2017). Sulfate to chloride ratios (SO_4^{2-}:Cl^-) were more similar to the nearby coastal sea value (0.0515) (Gondwe et al., 2010; Perry et al., 2002; Pohlman and Brankovits, 2017) than other settings in the Yucatán region (Gondwe et al., 2010; Perry et al., 2002). The highest SO_4^{2-}:Cl^- values (as high as 0.064) and highest degree of deviation from the seawater were observed in the BW. By contrast, the FW had the lowest SO_4^{2-}:Cl^- values (as low as 0.030), but these ratios were still in closer agreement with the seawater value than those in the BW. The SG SO_4^{2-}:Cl^- ratios were indistinguishable from the coastal seawater (Fig. 6). All geochemical data are available in the Appendix (Supplementary Data).

Conservative mixing and kinetic isotope models

The deviation between the conservative mixing model results with the measured values across the low-salinity-halocline reveals that a methane removal process imparting positive isotopic fractionation on the residual methane was active (Fig. 7a-b). The shaded area between the endmembers indicates where the constituents would physically mix in the absence of biological and/or chemically mediated inputs or removal. According to the mass balance calculations, 98.9% (or ~6,560 nM) of the methane was consumed within the low-salinity-halocline in January 2015, and 98.8% (or ~3,100 nM) in the January 2016. Despite different halocline depths and thicknesses for

379 the two sampling events, the percent removal of methane within the interface was
380 similar. By contrast, we conclude that no significant amount of methane is removed
381 within the high-salinity-halocline, where methane concentrations are uniformly low in
382 the BW and SG near the interface (Fig. 7a).
383 Our data more accurately matched the closed-system Rayleigh model than the
384 open-system model (Fig. 8), indicating that microbial methane oxidation within the
385 gradient zone is the primary process affecting the δ^{13}C-CH_4 values. Based on the
386 Rayleigh model, microbial methane oxidation removed up to ~99.0% (or ~7,700 nM) of
387 the methane source based on the January 2015 OPP profile, up to ~99.1% (or
388 ~4,300 nM) according to the January 2016 OPP profile, which agrees well with the
389 removal calculated by the mass balance approach using the conservative mixing model.
390
391 **DISCUSSION**
392 Pristine, cm-scale vertical sampling of salinity/density interfaces within flooded
393 cave passages provides valuable details about the distribution and reactivity of methane
394 within karst subterranean estuaries. Methane consumption was evident at the shallow
395 halocline between low salinity water masses (low-salinity-halocline), but not at the
396 deeper halocline between the meteoric lens and the saline groundwater (high-salinity-
397 halocline). These observations explain why manual sampling along m-scale vertical
398 profiles did not constrain the specific location where the oxidation of terrestrially-
399 derived methane occurs in this KSE (Brankovits et al., 2017). Our analysis of methane
400 concentrations and their δ^{13}C values along salinity gradients, using mixing models and
401 kinetic isotope models, identifies a generally uniform source of methane and a hotspot of
402 aerobic methane oxidation at the shallow low-salinity-halocline where anoxic freshwater
403 and hypoxic brackish water intersect.
404
405 *Halocline dynamics affect chemical gradients*
406 Consistent with meromictic conditions for this KSE (Beddows et al., 2007;
407 Brankovits et al., 2017), low-salinity- and high-salinity-haloclines were observed in the

2015 and 2016 sampling events (Fig. 2), but show distinct differences with respect to their structure and position in the water column. In January 2015, the thickness of shallow and deep haloclines were at least 12 cm less than in 2016, suggesting more stable conditions and less mixing in 2015. Also, the average approximate water depth of the low-salinity-halocline was ~40 cm deeper and the high-salinity-halocline was ~14 cm deeper during 2016 than in 2015, implying that the high groundwater level is associated with greater mixing. These observations are consistent with a previous study that found high precipitation prior to the 2016 sampling was associated with increased hydraulic head and groundwater flow, which enhances mixing (Brankovits et al., 2018). Indeed, the total precipitation during a 15-day time period preceding the sampling event was 39 mm in 2015 and 253 mm in 2016 (Brankovits et al., 2018). Temporal and spatial differences in precipitation patterns have a direct impact on the dynamic hydrology of karst aquifers which may directly affect mixing and, thus, water quality on short (Kovacs et al., 2017) and long timescales (Curtis et al., 1996; van Hengstum et al., 2010).

Sulfate to chloride ratios in close agreement with reported regional seawater values (0.0515) (Gondwe et al., 2010; Perry et al., 2002; Pohlman and Brankovits, 2017) are found throughout all profiles, which implies a marine origin for these ions and suggests physical mixing of fresh and marine-derived saline waters affects all three water layers. However, reduction in the SO_4^{2-}:Cl^- value (as low as 0.030), relative to the regional seawater value (0.0515), observed at the shallow halocline in 2015 (Fig. 5) is consistent with localized sulfate reduction. By contrast, increase in SO_4^{2-}:Cl^- values (as high as 0.064) and highest degree of deviation from the seawater value observed along the deep halocline (Fig. 6) implies an additional sulfate input, possibly from gypsum/anhydrite dissolution in the interior of the Yucatán platform (Perry et al., 2002).

Profiles across the low-salinity and high-salinity-haloclines show different trends in methane concentrations and $\delta^{13}C$ values. Methane source concentrations in the FW were higher in 2015 relative to those in 2016, but showed no substantial difference between source $\delta^{13}C$ values (as low as −67.51‰ in 2015 and −67.47‰ in 2016), indicating that methane accumulation was higher in 2015 than in 2016. Increased

437 mixing, as discussed above, might also result in lower methane accumulation in the
438 system. The pattern of increasing $\delta^{13}C$-CH_4 values with decreasing methane
439 concentrations across the low-salinity-halocline is a methane oxidation effect by either
440 anaerobic or aerobic methanotrophs (e.g., Barker and Fritz, 1981; Whiticar, 1999).
441 The presence of relatively high dissolved oxygen in the BW during 2015 (Fig. 2)
442 and other sampling campaigns (Brankovits et al., 2017) suggests aerobic methane
443 oxidation, the most thermodynamically-favorable oxidation pathway, was active during
444 this period (e.g., Whiticar, 1999). Although dissolved oxygen content was considerably
445 lower in the BW during January 2016 (1-10 µM) (Fig. 2), coastal sea studies have shown
446 that aerobic methane oxidation is possible under these conditions (Steinle et al., 2017).
447 Nevertheless, the low SO_4^{2-}:Cl^- value (0.030) observed at the shallow halocline in 2015
448 (Fig. 5a) is consistent with localized sulfate reduction proximal to where methane is
449 consumed, raising the possibility that anaerobic oxidation of methane may also be active
450 within the caves where oxygen is not available.
451 In contrast to the shallow profiles, the deeper high-salinity-halocline is associated
452 with no significant methane-removal mechanism as shown by the similar methane
453 concentrations during each deployment in the two water layers (Fig. 6). Higher methane
454 concentrations in 2015 than in 2016 at the high-salinity-halocline imply that periods of
455 greater methane accumulation in the FW source regime (2015 on Fig. 5) are associated
456 with higher residual methane concentrations in deeper waters. Although these
457 observations are consistent with physical mixing as the key factor affecting the
458 distribution of methane-related chemical properties across the deep interface, the
459 measured values do not all fall on the conservative mixing field (Fig. 7). Such pattern
460 suggests that additional processes may affect methane at the deeper mixing zone. For
461 example, the depleted $\delta^{13}C$ values in the SG relative to those in the BW (Fig. 7b) raise
462 the possibility for another methane source in the SG.
463

Multi-model approach confirms methanotrophy

The concentration-based conservative mixing model (Fig. 7a) further indicates the observed reduction in methane concentrations at the low-salinity-halocline was affected by methane removal; not only the physical mixing of low and high salinity waters. The extreme shift in δ^{13}C-CH_4 values for the isotopic mixing model (Fig. 7b) strongly suggests the reduction of methane across this interface is coupled with isotopic fractionation that occurs during microbial methane oxidation (Barker and Fritz, 1981; Whiticar, 1999). High-resolution sampling of the entire salinity gradient made it possible to demonstrate that methane oxidation is occurring strictly at the low-salinity-halocline. This evidence suggests that methanotrophic bacteria responsible for introducing methane carbon into the food web in this habitat (Brankovits et al., 2017) are concentrated at this interface. Evidence for additional input of sulfate near the high-salinity-halocline, as implied from SO_4^{2-}:Cl^- values, suggests that mixing processes are more complex in the flooded coastal caves than assumed by the conservative mixing model, which assumes the local mixing regime consists of FW and the marine-derived SG, with BW being a mixture of these endmembers. As a result, we use kinetic isotope models as an alternate approach to investigate methane oxidation dynamics across the low-salinity-halocline, where methane consumption is evident from the profiles.

A comparison of the closed- and open-system kinetic isotope models demonstrates that the measured methane concentrations and isotopic values are most similar to the values predicted by the closed-system isotope model (Fig. 8). This observation provides additional, robust evidence that the variability in measured methane isotopic ratios is primarily due to microbial oxidation, with minimal influence by mixing and external inputs, and that the methane originates from a generally uniform source located nearby the cave ceiling. Considering the strictly anoxic conditions required for the production of methane with a source δ^{13}C signature as low as −67.5‰, our previous studies concluded that methane production takes place in the anoxic saturated soil/rock-matrix overlying the cave passages (Brankovits et al., 2017, 2018). The downward migration of methane from nearby soils is consistent with the distribution

493 of terrestrial origin dissolved organic carbon (δ^{13}C-DOC = −28.0‰) in this environment
494 (Brankovits et al., 2017).
495 Assuming the lowest measured δ^{13}C-CH_4 value (R_0 = −67.5‰) is the source
496 signature, and using the isotope fractionation factor determined by the Rayleigh model,
497 it was possible to estimate the corresponding FW endmember concentration for each
498 measured methane concentration value from the low-salinity-halocline profiles. These
499 calculations predict the average source methane concentrations were ~8,700 nM in 2015
500 and ~5,200 nM in 2016. The difference between the calculated endmember methane
501 concentrations for the two sampling periods is consistent with there being higher
502 methane accumulation in the FW below the cave ceiling in 2015 than in 2016.
503 Methanotrophy, however, removed a similar fraction of methane originating from the
504 FW in both years. The closed-system kinetic isotope model and the mass balance
505 calculations based on a conservative mixing model agree that at least 98% of available
506 methane was oxidized during both years, suggesting that microbial methane oxidation is
507 an efficient methane sink in the KSE's cave passages.
508
509 *Conclusions*
510 Methane released from overlying soil/rock-matrix into cave networks flooded by
511 the karst subterranean estuary is consumed at a 12-24 cm thick halocline located
512 between the methane-charged freshwater and the underlying brackish water layer that is
513 the major hydrologic pathway to the coast (Fig. 9). Here, aerobic methane oxidation is
514 the dominant process that creates a hotspot of methane consumption in the shallow
515 meteoric lens between the anoxic freshwater and the brackish water with elevated
516 oxygen concentrations. By contrast, we observed no evidence of significant methane
517 removal at the deeper halocline between the meteoric lens and the saline groundwater.
518 Mixing models and kinetic isotope models provide evidence for oxidative removal of at
519 least 98% of the methane originating from the freshwater layer during 2015 and 2016.
520 This observation contributes to the growing evidence that subterranean estuaries have a
521 role in greenhouse gas dynamics (Pain et al., 2019) and act as a methane sink

(Brankovits et al., 2018; Schutte et al., 2016), which affects the amount and type of methane emitted into the coastal ocean by submarine groundwater discharge. Biogeochemical processes affecting methane dynamics and the transformation of organic matter in the cave environment of the KSEs are particularly important because the vast networks of natural conduits provide direct pathway of terrestrial materials into the coastal sea (Gonneea et al., 2014; Young et al., 2008). Moreover, our findings demonstrate that caves in the phreatic zone of a karst system are capable of acting as a methane sink, similar to air-filled caves in the vadose zone (Fernandez-Cortes et al., 2015; Ojeda et al., 2019; Webster et al., 2018). Increasing collective evidence for methane consumption in a globally distributed environment should encourage future research in karst systems that may have a greater role in greenhouse gas dynamics than previously thought.

ACKNOWLEDGEMENTS

Funding for D.B. was provided by the Research-in-Residence program (NSF award #1137336, Inter-university Training in Continental-scale Ecology), the Boost Fellowship (Texas A&M University at Galveston) and the joint Postdoctoral Scholar Program by Woods Hole Oceanographic Institution and U.S. Geological Survey. We express our gratitude to Michael Casso (USGS) and Emile Bergeron (USGS) for their help with developing the OctoPiPi water sampler. Sean P. Sylva helped with laboratory analyses. We thank Jacob Pohlman, Jake Emmert and István Brankovits for assistance with field expeditions, and Moody Gardens (Galveston, Texas) for supporting the fieldwork. Special thanks to the late Bil Phillips (Speleotech) for helping our field operations in Mexico. Any use of trade names is for descriptive purposes and does not imply endorsement by the U.S. government. All data from this study are available as Supplementary Data.

APPENDIX: SUPPLEMENTARY DATA

Supplementary data associated with this article can be found in the online version.

551 **REFERENCES**

552 Alvarez, F., Iliffe, T.M., Benitez, S., Brankovits, D. and Villalobos, J.L. (2015) New
553 records of anchialine fauna from the Yucatan Peninsula, Mexico. *Check List* **11**,
554 1505.

555 Barker, J.F. and Fritz, P. (1981) Carbon isotope fractionation during microbial
556 methane oxidation. *Nature* **293**, 289-291.

557 Bastviken, D., Cole, J., Pace, M. and Tranvik, L. (2004) Methane emissions from
558 lakes: Dependence of lake characteristics, two regional assessments, and a global
559 estimate. *Global Biogeochemical Cycles* **18**.

560 Bastviken, D., Cole, J.J., Pace, M.L. and Van de Bogert, M.C. (2008) Fates of
561 methane from different lake habitats: Connecting whole-lake budgets and CH4
562 emissions. *Journal of Geophysical Research: Biogeosciences* **113**.

563 Bastviken, D., Ejlertsson, J., Sundh, I. and Tranvik, L. (2003) Methane as a source of
564 carbon and energy for lake pelagic food webs. *Ecology* **84**, 969-981.

565 Bastviken, D., Tranvik, L.J., Downing, J.A., Crill, P.M. and Enrich-Prast, A. (2011)
566 Freshwater methane emissions offset the continental carbon sink. *Science* **331**, 50-
567 50.

568 Bauer-Gottwein, P., Gondwe, B.R., Charvet, G., Marín, L.E., Rebolledo-Vieyra, M.
569 and Merediz-Alonso, G. (2011) the Yucatán Peninsula karst aquifer, Mexico.
570 *Hydrogeology Journal* **19**, 507-524.

571 Beck, A.J., Charette, M.A., Cochran, J.K., Gonneea, M.E. and Peucker-Ehrenbrink,
572 B. (2013) Dissolved strontium in the subterranean estuary - Implications for the
573 marine strontium isotope budget. *Geochimica et Cosmochimica Acta* **117**, 33-52.

574 Beddows, P.A., Smart, P.L., Whitaker, F.F. and Smith, S.L. (2007) Decoupled fresh-
575 saline groundwater circulation of a coastal carbonate aquifer: Spatial patterns of
576 temperature and specific electrical conductivity. *Journal of Hydrology* **346**, 18-32.

577 Bishop, R.E., Humphreys, W.F., Cukrov, N., Zic, V., Boxshall, G.A., Cukrov, M.,
578 Iliffe, T.M., Krsinic, F., Moore, W.S., Pohlman, J.W. and Sket, B. (2015)
579 'Anchialine' redefined as a subterranenan estuary in crevicular or cavernous
580 geological setting. *Journal of Crustacean Biology* **35**, 511-514.

581 Boetius, A. and Wenzhofer, F. (2013) Seafloor oxygen consumption fuelled by
582 methane from cold seeps. *Nature Geoscience* **6**, 725-734.

583 Brankovits, D., Pohlman, J., Ganju, N.K., Iliffe, T., Lowell, N., Roth, E., Sylva, S.,
584 Emmert, J. and Lapham, L. (2018) Hydrologic controls of methane dynamics in karst
585 subterranean estuaries. *Global Biogeochemical Cycles* **32**, 1759-1775.

586 Brankovits, D., Pohlman, J.W., Niemann, H., Leigh, M.B., Leewis, M.-C., Becker,
587 K.W., Iliffe, T.M., Alvarez, F., Lehmann, M.F. and Phillips, B. (2017) Methane-and
588 dissolved organic carbon-fueled microbial loop supports a tropical subterranean
589 estuary ecosystem. *Nature Communications* **8**, 1835.

590 Burnett, W., Aggarwal, P., Aureli, A., Bokuniewicz, H., Cable, J., Charette, M.,
591 Kontar, E., Krupa, S., Kulkarni, K. and Loveless, A. (2006) Quantifying submarine
592 groundwater discharge in the coastal zone via multiple methods. *Science of the Total*
593 *Environment* **367**, 498-543.

594 Cable, J.E., Bugna, G.C., Burnett, W.C. and Chanton, J.P. (1996) Application of
595 222Rn and CH4 for assessment of groundwater discharge to the coastal ocean.
596 *Limnology and Oceanography* **41**, 1347-1353.

597 Chanton, J.P. and Lewis, F.G. (1999) Plankton and dissolved inorganic carbon
598 isotopic composition in a river-dominated estuary: Apalachicola Bay, Florida.
599 *Estuaries* **22**, 575-583.

600 Corliss, J.B., Dymond, J., Gordon, L.I., Edmond, J.M., Herzen, R.P.V., Ballard,
601 R.D., Green, K., Williams, D., Bainbridge, A., Crane, K. and Vanandel, T.H. (1979)
602 Submarine thermal springs on the Galapagos Rift. *Science* **203**, 1073-1083.

603 Coutino, A., Stastna, M., Kovacs, S. and Reinhardt, E. (2017) Hurricanes Ingrid and
604 Manuel (2013) and their impact on the salinity of the Meteoric Water Mass,
605 Quintana Roo, Mexico. *Journal of Hydrology* **551**, 715-729.

606 Curtis, J.H., Hodell, D.A. and Brenner, M. (1996) Climate variability on the Yucatan
607 Peninsula (Mexico) during the past 3500 years, and implications for Maya cultural
608 evolution. *Quaternary Research* **46**, 37-47.

609 Damm, E., Schauer, U., Rudels, B. and Haas, C. (2007) Excess of bottom-released
610 methane in an Arctic shelf sea polynya in winter. *Continental Shelf Research* **27**,
611 1692-1701.

612 Deines, P., Wooller, M.J. and Grey, J. (2009) Unravelling complexities in benthic
613 food webs using a dual stable isotope (hydrogen and carbon) approach. *Freshwater*
614 *Biology* **54**, 2243-2251.

615 DelVecchia, A.G., Stanford, J.A. and Xu, X. (2016) Ancient and methane-derived
616 carbon subsidizes contemporary food webs. *Nature Communications* **7**, 13163.

Devlin, S.P., Saarenheimo, J., Syväranta, J. and Jones, R.I. (2015) Top consumer abundance influences lake methane efflux. *Nature Communications* **6**, 8787.

Fernandez-Cortes, A., Cuezva, S., Alvarez-Gallego, M., Garcia-Anton, E., Pla, C., Benavente, D., Jurado, V., Saiz-Jimenez, C. and Sanchez-Moral, S. (2015) Subterranean atmospheres may act as daily methane sinks. *Nature Communications* **6**, 7003.

Ford, D. and Williams, P.D. (2013) *Karst Hydrogeology and Geomorphology*. John Wiley & Sons, West Sussex.

Gondwe, B.R., Lerer, S., Stisen, S., Marín, L., Rebolledo-Vieyra, M., Merediz-Alonso, G. and Bauer-Gottwein, P. (2010) Hydrogeology of the south-eastern Yucatan Peninsula: new insights from water level measurements, geochemistry, geophysics and remote sensing. *Journal of Hydrology* **389**, 1-17.

Gonneea, M.E., Charette, M.A., Liu, Q., Herrera-Silveira, J.A. and Morales-Ojeda, S.M. (2014) Trace element geochemistry of groundwater in a karst subterranean estuary (Yucatan Peninsula, Mexico). *Geochimica et Cosmochimica Acta* **132**, 31-49.

Gonzalez, B.C., Iliffe, T.M., Macalady, J.L., Schaperdoth, I. and Kakuk, B. (2011) Microbial hotspots in anchialine blue holes: initial discoveries from the Bahamas. *Hydrobiologia* **677**, 149-156.

Grey, J. (2016) The incredible lightness of being methane-fuelled: stable isotopes reveal alternative energy pathways in aquatic ecosystems and beyond. *Frontiers in Ecology and Evolution* **4,** 8.

He, R., Wooller, M.J., Pohlman, J.W., Tiedje, J.M. and Leigh, M.B. (2015) Methane-derived carbon flow through microbial communities in arctic lake sediments. *Environmental Microbiology* **17**, 3233-3250.

Humphreys, W. (1999) Physico-chemical profile and energy fixation in Bundera Sinkhole, an anchialine remiped habitat in north-western Australia. *Journal of the Royal Society of Western Australia* **82**, 89-98.

Iliffe, T.M. and Kornicker, L.S. (2009) Worldwide diving discoveries of living fossil animals from the depths of anchialine and marine caves. *Smithsonian Contributions to Marine Sciences* **38**, 269-280.

IPCC (2014) *Climate Change 2014–Impacts, Adaptation and Vulnerability: Regional Aspects*. Cambridge University Press.

650 Kambesis, P.N. and Coke, J.G. (2013) *Overview of the controls on eogenetic cave*
651 *and karst development in Quintana Roo, Mexico, Coastal Karst Landforms*.
652 Springer, pp. 347-373.

653 Kessler, J., Reeburgh, W. and Tyler, S. (2006) Controls on methane concentration
654 and stable isotope (δ2H-CH4 and δ13C-CH4) distributions in the water columns of
655 the Black Sea and Cariaco Basin. *Global Biogeochemical Cycles* **20**.

656 Kottek, M., Grieser, J., Beck, C., Rudolf, B. and Rubel, F. (2006) World map of the
657 Köppen-Geiger climate classification updated. *Meteorologische Zeitschrift* **15**, 259-
658 263.

659 Kovacs, S.E., Reinhardt, E.G., Stastna, M., Coutino, A., Werner, C., Collins, S.V.,
660 Devos, F. and Le Maillot, C. (2017) Hurricane Ingrid and Tropical Storm Hanna's
661 effects on the salinity of the coastal aquifer, Quintana Roo, Mexico. *Journal of*
662 *Hydrology* **551**, 703-714.

663 Kroeger, K. and Charette, M. (2008) Nitrogen biogeochemistry of submarine
664 groundwater discharge. *Limnology and Oceanography* **53**, 1025-1039.

665 Kwon, E.Y., Kim, G., Primeau, F., Moore, W.S., Cho, H.M., DeVries, T., Sarmiento,
666 J.L., Charette, M.A. and Cho, Y.K. (2014) Global estimate of submarine
667 groundwater discharge based on an observationally constrained radium isotope
668 model. *Geophysical Research Letters* **41**, 8438-8444.

669 Lee, Y.W., Kim, G., Lim, W.A. and Hwang, D.W. (2010) A relationship between
670 submarine groundwater-borne nutrients traced by Ra isotopes and the intensity of
671 dinoflagellate red-tides occurring in the southern sea of Korea. *Limnology and*
672 *Oceanography* **55**, 1-10.

673 Leonte, M., Kessler, J.D., Kellermann, M.Y., Arrington, E.C., Valentine, D.L. and
674 Sylva, S.P. (2017) Rapid rates of aerobic methane oxidation at the feather edge of
675 gas hydrate stability in the waters of Hudson Canyon, US Atlantic Margin.
676 *Geochimica et Cosmochimica Acta* **204**, 375-387.

677 Levin, L.A. (2005) Ecology of cold seep sediments: interactions of fauna with flow,
678 chemistry and microbes. *Oceanography and Marine Biology: An Annual Review* **43**,
679 1-46.

680 Magen, C., Lapham, L.L., Pohlman, J.W., Marshall, K., Bosman, S., Casso, M. and
681 Chanton, J.P. (2014) A simple headspace equilibration method for measuring
682 dissolved methane. *Limnology and Oceanogaphy: Methods* **12**, 637-650.

683 Martin, J.B., Gulley, J. and Spellman, P. (2012) Tidal pumping of water between
684 Bahamian blue holes, aquifers, and the ocean. *Journal of Hydrology* **416**, 28-38.

685 Moore, W.S. (1999) The subterranean estuary: a reaction zone of ground water and
686 sea water. *Marine Chemistry* **65**, 111-125.

687 Moore, W.S. (2010) The effect of submarine groundwater discharge on the ocean.
688 *Annual Review of Marine Science* **2**, 59-88.

689 Ojeda, L., Vadillo, I., Etiope, G., Benavente, J., Liñán, C., del Rosal, Y., Tapia, S.T.,
690 Moríñigo, M.Á. and Carrasco, F. (2019) Methane sources and sinks in karst systems:
691 the Nerja cave and its vadose environment (Spain). *Geochimica et Cosmochimica*
692 *Acta* **259**, 302-315.

693 Pain, A.J., Martin, J.B. and Young, C.R. (2019) Sources and sinks of CO2 and CH4
694 in siliciclastic subterranean estuaries. *Limnology and Oceanography* **64**, 1500-1514.

695 Paull, C.K., Hecker, B., Commeau, R., Freemanlynde, R.P., Neumann, C., Corso,
696 W.P., Golubic, S., Hook, J.E., Sikes, E. and Curray, J. (1984) Biological
697 communities at the Florida escarpment resemble hydrothermal vent taxa. *Science*
698 **226**, 965-967.

699 Perry, E., Velazquez-Oliman, G. and Marin, L. (2002) The hydrogeochemistry of the
700 karst aquifer system of the northern Yucatan Peninsula, Mexico. *International*
701 *Geology Review* **44**, 191-221.

702 Pohlman, J.W. (2011) The biogeochemistry of anchialine caves: progress and
703 possibilities. *Hydrobiologia* **677**, 33-51.

704 Pohlman, J.W. and Brankovits, D. (2017) Water column physical and chemical
705 properties of Cenote Bang, a component of the Ox Bel Ha cave network within the
706 subterranean estuary coastal aquifer of the Yucatan Peninsula, from December 2013
707 to January 2016. *U.S. Geological Survey data release,*
708 https://doi.org/10.5066/F7DJ5DJW.

709 Pohlman, J.W., Iliffe, T.M. and Cifuentes, L.A. (1997) A stable isotope study of
710 organic cycling and the ecology of an anchialine cave ecosystem. *Marine Ecology*
711 *Progress Series* **155**, 17-27.

712 Pohlman, J.W., Ruppel, C., Hutchinson, D.R., Downer, R. and Coffin, R.B. (2008)
713 Assessing sulfate reduction and methane cycling in a high salinity pore water system
714 in the northern Gulf of Mexico. *Marine and Petroleum Geology* **25**, 942-951.

715 Popp, B.N., Sansone, F.J., Rust, T.M. and Merritt, D.A. (1995) Determination of
716 concentration and carbon isotopic composition of dissolved methane in sediments
717 and nearshore waters. *Analytical Chemistry* **67**, 405-411.

718 Reeburgh, W.S. (2007) Oceanic methane biogeochemistry. *Chemical Reviews* **107**,
719 486-513.

720 Santoro, A.E. (2010) Microbial nitrogen cycling at the saltwater-freshwater interface.
721 *Hydrogeology Journal* **18**, 187-202.

722 Santoro, A.E., Francis, C.A., de Sieyes, N.R. and Boehm, A.B. (2008) Shifts in the
723 relative abundance of ammonia-oxidizing bacteria and archaea across
724 physicochemical gradients in a subterranean estuary. *Environmental Microbiology*
725 **10**, 1068-1079.

726 Schutte, C.A., Wilson, A.M., Evans, T., Moore, W.S. and Joye, S.B. (2016)
727 Methanotrophy controls groundwater methane export from a barrier island.
728 *Geochimica et Cosmochimica Acta* **179**, 242-256.

729 Seymour, J., Humphreys, W. and Mitchell, J. (2007) Stratification of the microbial
730 community inhabiting an anchialine sinkhole. *Aquatic Microbial Ecology* **50**, 11-24.

731 Socki, R.A., Perry, E.C. and Romanek, C.S. (2002) Stable isotope systematics of two
732 cenotes from the northern Yucatan Peninsula, Mexico. *Limnology and*
733 *Oceanography* **47**, 1808-1818.

734 Steinle, L., Maltby, J., Treude, T., Kock, A., Bange, H.W., Engbersen, N., Zopfi, J.,
735 Lehmann, M.F. and Niemann, H. (2017) Effects of low oxygen concentrations on
736 aerobic methane oxidation in seasonally hypoxic coastal waters. *Biogeosciences* **14**,
737 1631-1645.

738 Stock, J.H., Iliffe, T.M. and Williams, D. (1986) The concept of anchialine
739 reconsidered. *Stygologia* **2**, 90-92.

740 Taniguchi, M., Burnett, W.C., Cable, J.E. and Turner, J.V. (2002) Investigation of
741 submarine groundwater discharge. *Hydrological Processes* **16**, 2115-2129.

742 van Hengstum, P.J., Reinhardt, E.G., Beddows, P.A. and Gabriel, J.J. (2010)
743 Linkages between Holocene paleoclimate and paleohydrogeology preserved in a
744 Yucatan underwater cave. *Quaternary Science Reviews* **29**, 2788-2798.

745 van Hengstum, P.J., Scott, D.B., Grocke, D.R. and Charette, M.A. (2011) Sea level
746 controls sedimentation and environments in coastal caves and sinkholes. *Marine*
747 *Geology* **286**, 35-50.

748 Vesper, D.J., Loop, C.M. and White, W.B. (2001) Contaminant transport in karst
749 aquifers. *Theoretical and Applied Karstology* **13**, 101-111.

Webster, K.D., Drobniak, A., Etiope, G., Mastalerz, M., Sauer, P.E. and Schimmelmann, A. (2018) Subterranean karst environments as a global sink for atmospheric methane. *Earth and Planetary Science Letters* **485**, 9-18.

Wetzel, R.G. (2001) *Limnology: Lake and River Ecosystems*. Gulf Professional Publishing.

White, D.A. and Hood, C.S. (2004) Vegetation patterns and environmental gradients in tropical dry forests of the northern Yucatan Peninsula. *Journal of Vegetation Science* **15**, 151-160.

Whiticar, M.J. (1999) Carbon and hydrogen isotope systematics of bacterial formation and oxidation of methane. *Chemical Geology* **161**, 291-314.

Young, M.B., Gonneea, M.E., Fong, D.A., Moore, W.S., Herrera-Silveira, J. and Paytan, A. (2008) Characterizing sources of groundwater to a tropical coastal lagoon in a karstic area using radium isotopes and water chemistry. *Marine Chemistry* **109**, 377-394.

Figures and Captions

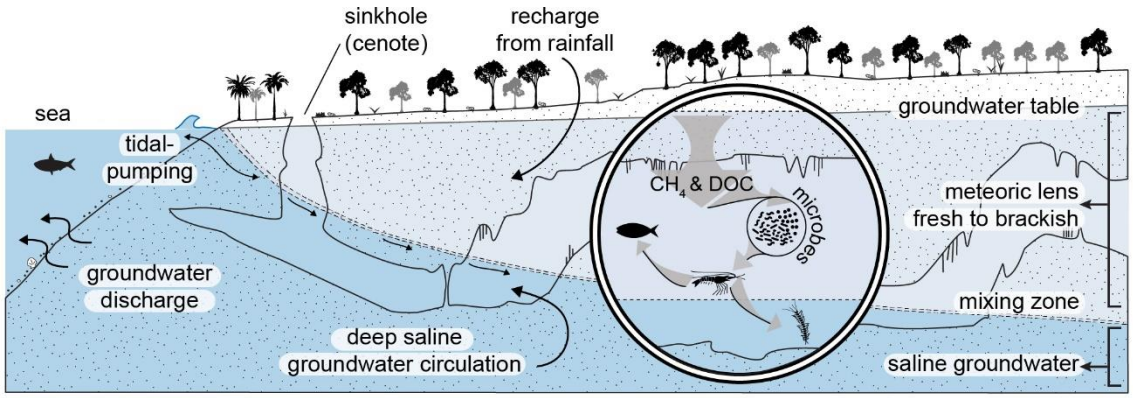

Figure 1: Conceptual model of the karst subterranean estuary (KSE) in an unconfined coastal aquifer setting. Mixing between freshwater and marine-derived saline groundwater occurs within the aquifer's porous geologic setting, including its sinkholes and cave conduits. Mixing zone (halocline) dynamics are controlled by density stratification, sea level, and other hydrologic processes. In this setting, a subterranean microbial loop (inset circle) transfers carbon from methane (CH_4) and dissolved organic carbon (DOC) formed by decomposition of terrestrial vegetation into the *anchialine* food web (Brankovits et al., 2017). Methane accumulation and consumption in the shallow portion of the aquifer are controlled by rainfall and hydrologic processes (Brankovits et al., 2018).

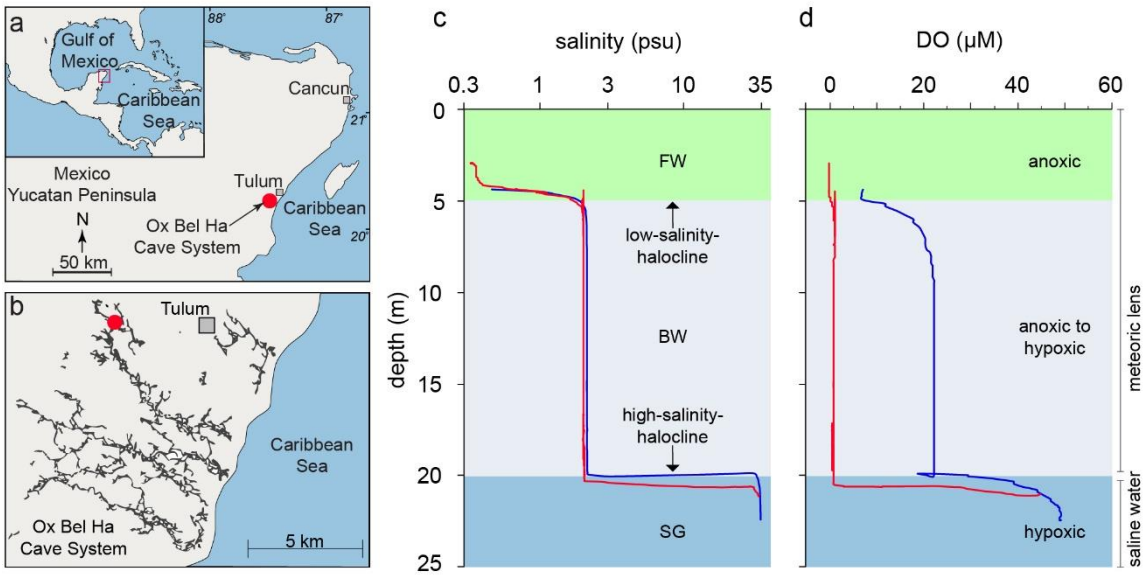

Figure 2: Field site and general vertical structure of the water column in a cave passage flooded by the groundwater. (a) The study site is located in the Yucatán Peninsula, Mexico. (b) Map of Ox Bel Ha Cave System showing explored cave passages that provide access to the subterranean estuary. The study site (red dot) is located 6.6 km inland from the coast. Physicochemical profiles obtained with a multi-parameter data sonde in January 2015 (blue line) and January 2016 (red line) as part of a preceding study (Brankovits et al., 2017) show (c) salinity and (d) dissolved oxygen (DO) along a depth profile. A shallow, low-salinity-halocline within the meteoric lens separates the anoxic freshwater (FW) from brackish water (BW), where DO concentrations were slightly higher, varying from anoxic to hypoxic conditions depending on the sampling season. The deeper, high-salinity-halocline separates the meteoric lens from the saline groundwater (SG).

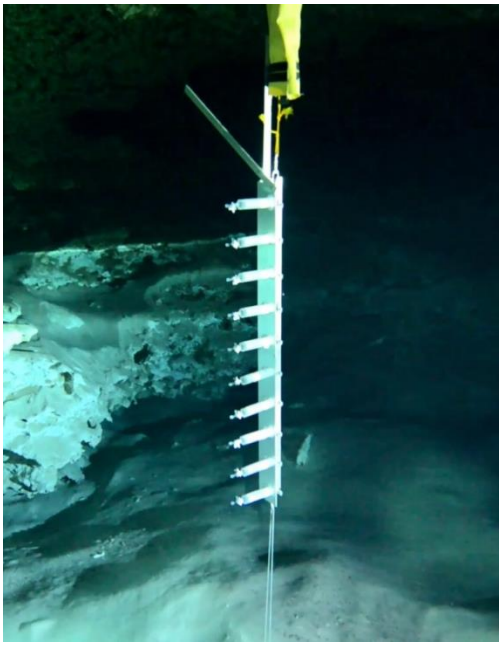

Figure 3: The OctoPiPi (OPP) deployed for sample collection in the water column of a flooded cave passage. The OPP contains ten 60 ml syringes that are distributed 12 cm vertically from each other. A smaller mini-OPP, which contained ten 60 ml syringes distributed 2.5 cm from each other, required a similar deployment procedure.

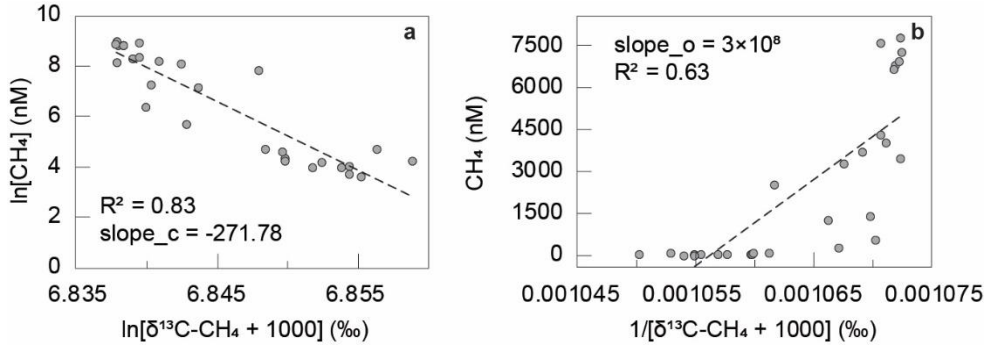

Figure 4: Methane concentration values plotted with values derived from the δ^{13}C-CH_4 ratios for the (a) Rayleigh and (b) open-system models. The slopes of the linear regressions were used to calculate the fractionation factor (α) for the Rayleigh and open-system kinetic isotope models from $slope_c = \alpha_c / (1 - \alpha_c)$ and $slope_o = -(\alpha_o (\delta R_0 + 1000) C_o) / (1 - \alpha_o)$ based on Eq. (3) and Eq. (4).

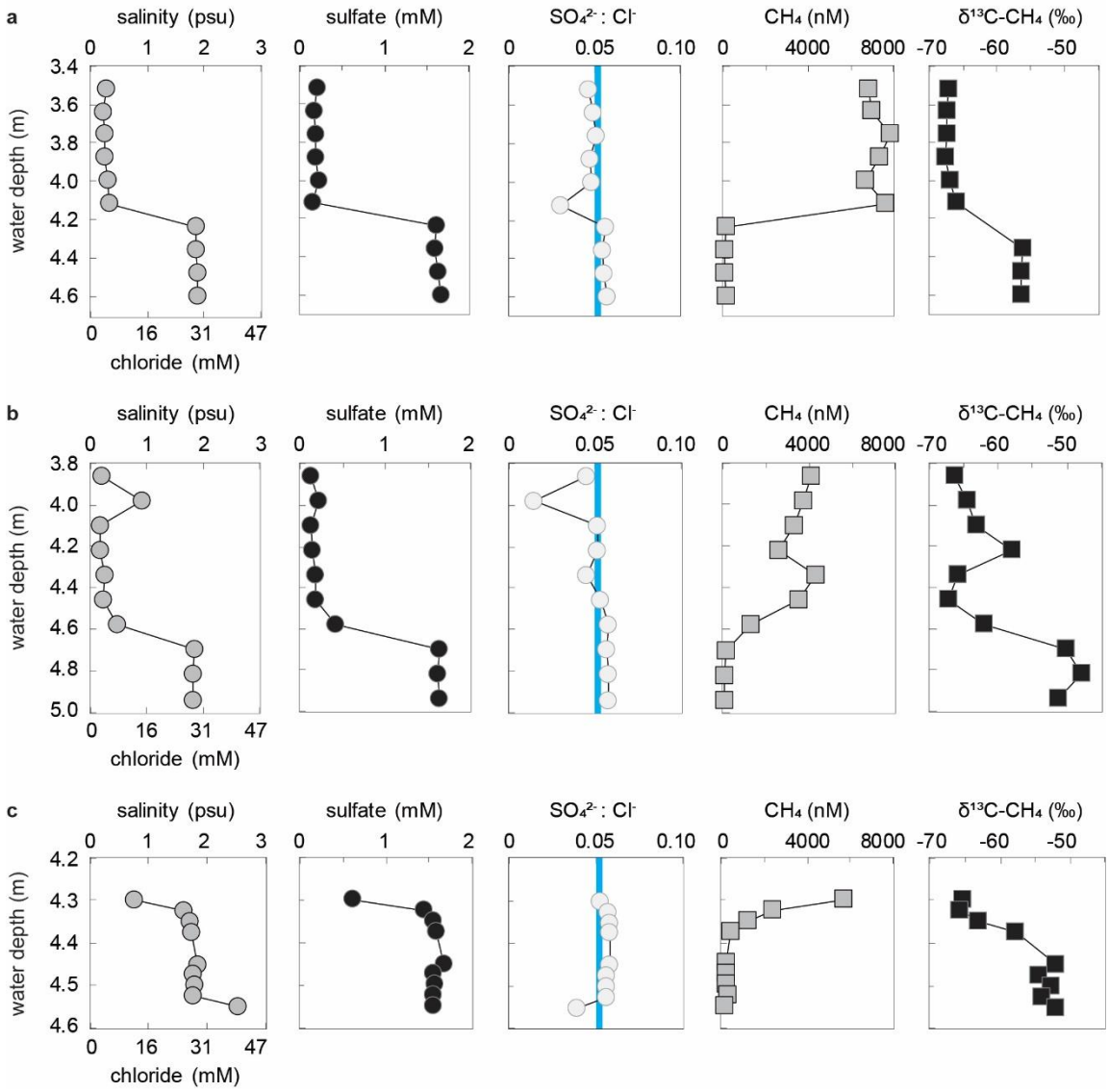

Figure 5: High-resolution depth profiles of chemical constituents across the low-salinity-halocline between the freshwater (FW) and brackish water (BW) layers. Samples were collected with the OPP in (a) January 2015 and (b) January 2016, as well as with the mini-OPP (c) in January 2016. Symbols of individual data points contain the analytical uncertainty (std. dev.) of the measured values. The blue line is the SO_4^{2-}:Cl^- ratio (0.0515) of the regional seawater.

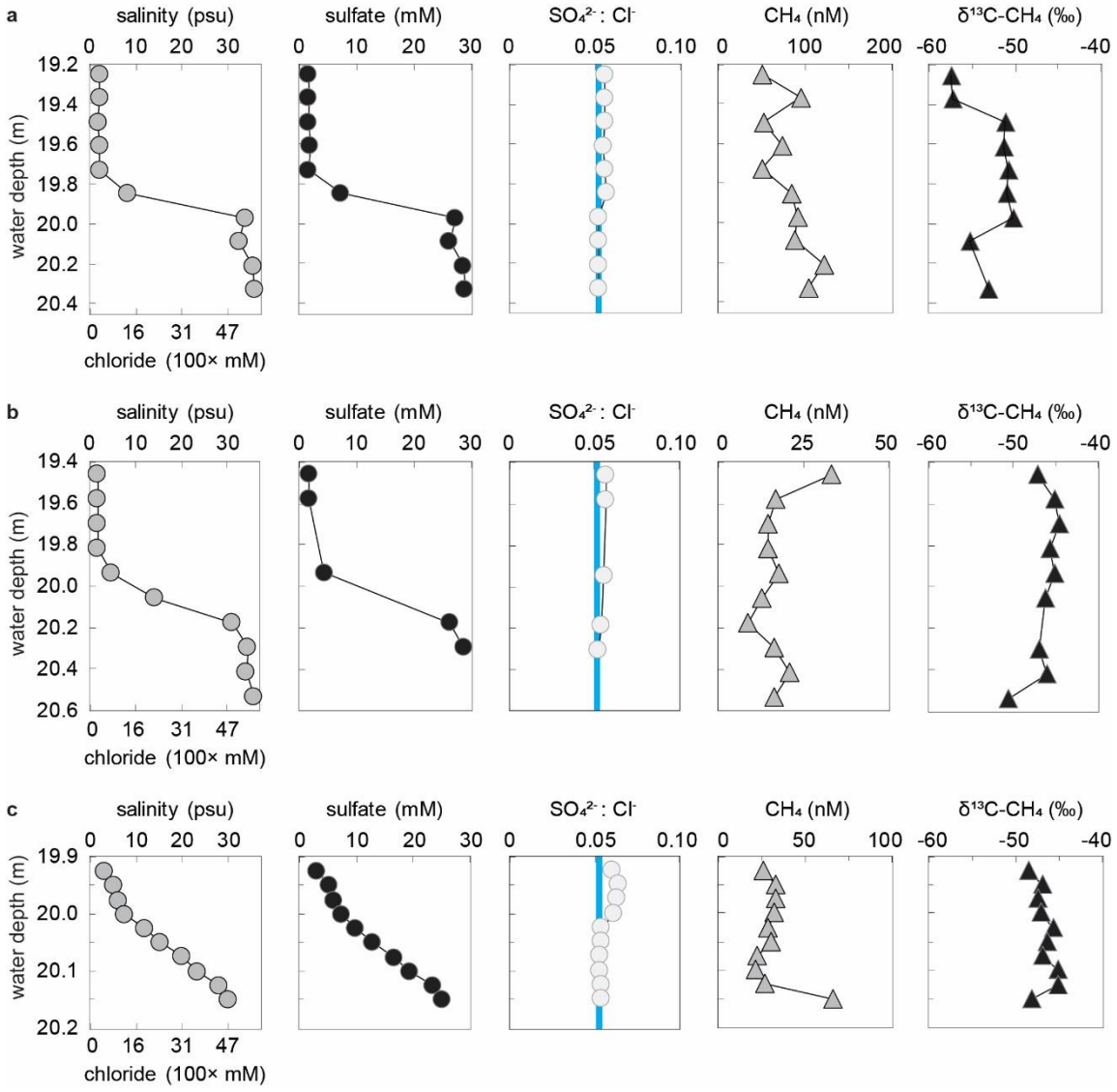

Figure 6: High-resolution depth profiles of chemical constituents across the high-salinity-halocline between the brackish water (BW) and saline groundwater (SG). Samples were collected with the OPP in (a) January 2015 and (b) January 2016, as well as with the mini-OPP (c) in January 2016. Symbols of individual data points contain the analytical uncertainty (std. dev.) of the measured values. The blue line is the SO_4^{2-}:Cl^- ratio (0.0515) of the regional seawater.

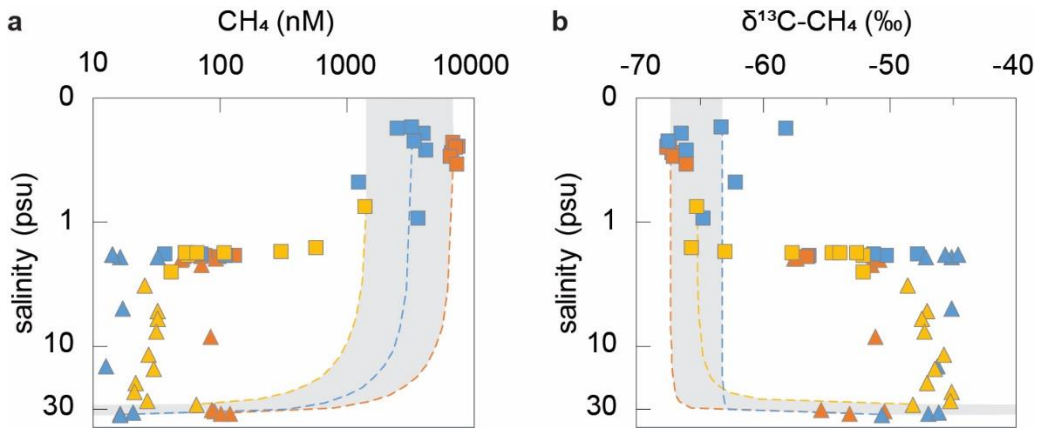

Figure 7: Salinity-property plots and the conservative mixing model output. (a) Salinity and methane concentrations plotted on log-scale. (b) Salinity and δ^{13}C-CH_4 values, with salinity plotted on log-scale. Colors indicate January 2015 (orange) and January 2016 (blue) OPP-deployments, and the January 2016 (yellow) mini-OPP deployment. Samples obtained from the low-salinity-halocline indicated as squares, and samples obtained from the high-salinity-halocline indicated as triangles. Colored dotted lines are conservative mixing model results for their respective event and represent the expected distribution when there is physical mixing only (no reactions). Grey area is the total area of the conservative mixing results. Depletion of the measured constituent relative to the concentration-based model suggests consumption of methane within the salinity transition. Deviation of the δ^{13}C-CH_4 values toward more positive values within the region of consumption corroborates that methane oxidation was active. Symbol of individual data points contain the analytical uncertainty (std. dev,) of each measurement.

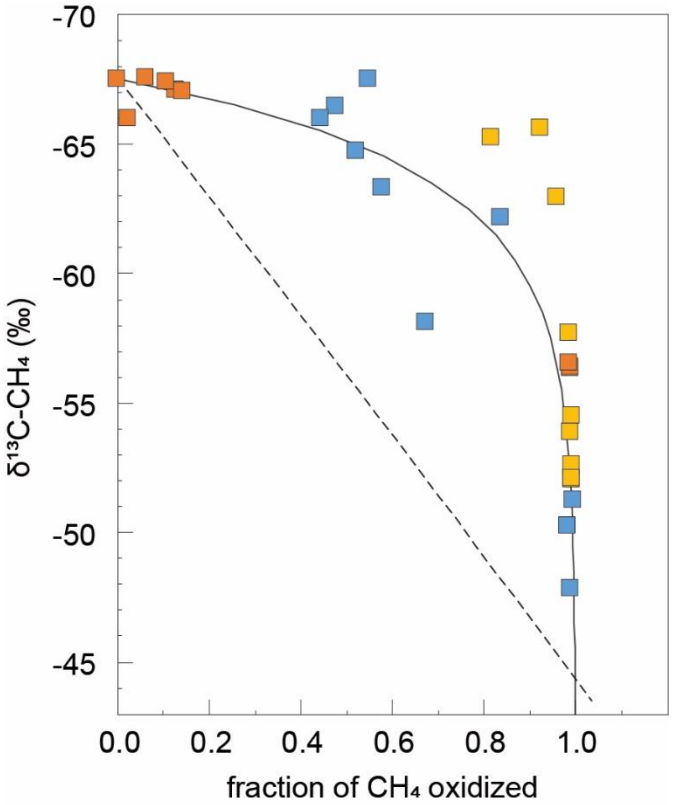

Figure 8: Measured δ^{13}C-CH_4 values plotted against the calculated fractions of methane oxidized. Colors indicate January 2015 (orange) and January 2016 (blue) OPP-deployments, and the January 2016 (yellow) mini-OPP deployment. The fraction of methane oxidized for the collected samples was calculated as $f = 1 - C/C_0$ where C is the methane concentration of each sample collected across the low-salinity-halocline and C_0 (7,544 nM) is the concentration of the unoxidized FW endmember (see methods for more details). These values are compared to model predictions from the closed-system model calculated using Eq. 1 (sold line) and the open-system calculated using Eq. 2 (dotted line) models. The closed-system model more closely matches the data than the open-system model.

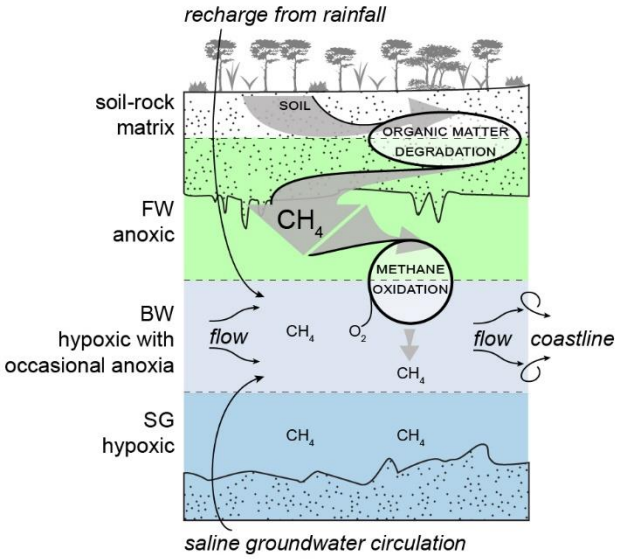

Figure 9: A conceptual model for methane oxidation within flooded cave conduits in a karst subterranean estuary. The carbonate rock (dotted area) and the cave passages (plain area) are saturated by the stratified groundwater of fresh (FW), brackish (BW), and saline (SG) waters. Methane transferred into the cave environment is removed by aerobic methane oxidation at the interface of anoxic FW and the generally hypoxic BW. Localized anaerobic conditions may also promote anaerobic methane oxidation by the reduction of sulfate that originates from the marine-derived SG. Overall, a hotspot of methane oxidation exists at the interface between anoxic methane-charged waters and hypoxic, higher salinity groundwater. This process removes much of the methane before its hydrologic transport to the coastal ocean.